

Multi-Node ML Time and Frequency Synchronization for Distributed MIMO-Relay Beamforming Over Time-Varying Flat-Fading Channels

Souheib Ben Amor¹, Sofiène Affes¹, *Senior Member, IEEE*, Faouzi Bellili²,
Usa Vilaipornsawai, Liqing Zhang, and Peiying Zhu, *Fellow, IEEE*

Abstract—In this paper, we investigate maximum likelihood (ML) time delay (TD) and carrier frequency offset (CFO) synchronization in multi-node decode-and-forward cooperative relaying systems operating over time-varying channels. This new synchronization scheme is embedded into a distributed multiple input multiple output (MIMO)-relay beamforming transceiver structure to avoid the drawbacks of multidimensional ML estimation at the destination and to minimize the overhead cost. By accounting for a perfect Doppler spread value, the new synchronization solution delivers accurate TD and CFO estimates. For real-world operation, however, this new technique can be jointly implemented with any Doppler spread estimator in a new iterative scheme using a time-constant channel (TCC)-based synchronization method at the initialization step. The resulting TD and CFO estimates along with the channel estimates are then fed into a distributed MIMO-relay beamforming transceiver of K single-antenna nodes, for pre-compensation at each node of the transmitted signals, to ensure constructive maximum ratio combining (MRC) at the destination. Simulation results show significant synchronization accuracy improvement over previous distributed multi-node synchronization techniques assuming TCCs. The latter translates into noticeable gains in terms of useful link-level throughput, more so at higher Doppler or with more relaying nodes.

Index Terms—Carrier frequency offset (CFO), time delay (TD), time-varying channel (TVC), Doppler spread, dis-

tributed MIMO relay beamforming, cooperation, collaboration, decode-and-forward (DF), multi-node synchronization, maximum likelihood (ML).

I. INTRODUCTION

SPATIAL diversity is a well-known concept allowing to combat the channel fading and increase the overall throughput of communication systems. Such attracting advantage can be achieved through multiple solutions. Cooperative networks provide a distributed solution that avoids some of the difficulties related to traditional multiple input multiple output (MIMO) systems [2], [3]. Indeed, in many situations, some user equipments are not able to embed multiple antenna sensors due to size and power limitations. As such, users can cooperate with each other to form a virtual antenna array. However, some challenges need to be addressed to ensure constructive cooperation between the relays. One major problem in cooperative relaying systems is multi-node synchronization, both in time and frequency. The latter is crucial for the proper implementation of energy-, spectrum-, and area-efficient distributed MIMO-relay beamforming between a given source-destination link having coverage limitations.

There are two basic approaches to alleviate the effect of time-varying channel (TVC) distortions in time, frequency, phase, and amplitude: the closed-loop and the open-loop compensation procedures. In the closed-loop approach, the destination performs the estimation of all the synchronization parameters along with the channel coefficients. Those estimates are later fed to an equalization block to combat time and frequency asynchronism as proposed in [4] and [5]. To their credentials, closed-loop approaches exhibit less overhead as the interaction among the relay nodes is kept to minimal while the destination coordinates the synchronization process. However, it may be difficult for wireless networks without the adequate infrastructure to handle highly-complex multi-dimensional estimation algorithms. In open-loop approaches, however, the source signal to be relayed is shifted in the temporal and frequency domains before transmission, as proposed in [6]. By doing so, we ensure that replicas of the same transmitted signal, originating from different relay nodes, arrive at the same time and combine constructively at the receiver. In this scenario, less complex estimation algorithms

Manuscript received June 21, 2018; revised September 14, 2018 and November 6, 2018; accepted December 1, 2018. Date of publication December 21, 2018; date of current version April 16, 2019. Work supported by the NSERC/Huawei Canada/TELUS CRD Grant on 5G-WAVES (Wireless Access Virtualization Enabling Schemes), the DG and CREATE PERSWADE <www.create-perswade.ca> Programs of NSERC, and a Discovery Accelerator Supplement Award from NSERC. This paper was presented in part at the IEEE GLOBECOM'2018 [1]. The associate editor coordinating the review of this paper and approving it for publication was D. B. Da Costa. (*Corresponding author: Souheib Ben Amor.*)

S. B. Amor and S. Affes are with INRS-EMT, Université du Québec, Montréal, QC H2L 2C4, Canada (e-mail: souheib.ben.amor@emt.inrs.ca; affes@emt.inrs.ca).

F. Bellili is with the Department of Electrical and Computer Engineering, University of Manitoba, Winnipeg, MB R3T 2N2, Canada (e-mail: faouzi.bellili@umanitoba.ca).

U. Vilaipornsawai, L. Zhang, and P. Zhu are with the Huawei Technologies Canada Co. Ltd., Markham, ON L3R 5A4, Canada (e-mail: usa.vilaipornsawai@huawei.com; liqing.zhang@huawei.com; peiying.zhu@huawei.com).

Color versions of one or more of the figures in this paper are available online at <http://ieeexplore.ieee.org>.

Digital Object Identifier 10.1109/TCOMM.2018.2889089

can be considered at the nodes with minimal signaling from the destination.

As far as the estimation of the synchronization parameters is concerned, multiple techniques exist in the open literature [7]. On one hand, the works in [8]–[11] investigate time delay (TD) synchronization while neglecting the carrier frequency offset's (CFO) effect. On the other hand, the solutions introduced in [12]–[14] deal with multiple CFOs while neglecting the TD effect. Other techniques perform joint estimation of all parameters at the destination in closed-loop cooperative networks [4], [15], [16]. Although they could work well in practice, they suffer from high computational complexity since they require solving a multi-dimensional problem that increases with the number of relaying nodes. Moreover, the synchronization task might become very costly in terms of overhead. Indeed, after estimating the TDs and CFOs, the destination node needs to feed them back to the relays. Such a step leads to an additional overhead problem along with quantization errors since the estimated values are quantized before their feedback phase.

Alternative solutions can be considered by relying on distributed collaborative beamforming (DCBF) schemes [17]. Many of these techniques focus on the optimal design of the beamformer's weights while assuming perfect synchronization that leave them extremely vulnerable in practice to phase, frequency, and time offsets. Many other techniques focus on the other hand on combating the misalignment effect at the destination caused by such offsets. Yang *et al.* [18] proposed a phase compensation solution based on an iterative bit-feedback approach. In [19], a solution for frequency synchronization in wireless sensor networks (WSN) using a round trip synchronization method was proposed. In [20], a distributed synchronization method was proposed for dense wireless networks using a correlation-based joint TD and CFO estimator. Yet, all the above-mentioned techniques rely on the simplifying time-constant channel (TCC) assumption. In contrast, a broad range of applications require that the terminals act as relaying nodes and, at the same time, fifth-generation (5G) communication systems are expected to support reliable communications at very high velocities reaching 500 Km/h (e.g., in high-speed trains) [21]. For such systems, the conventional TCC assumption leads to severe performance losses. Recently, some other works on DCBF [22], [23] had tackled the challenging problem of multi-node synchronization under TVCs using enhanced versions of one-bit feedback technique. However, they have only addressed phase compensation while assuming perfect TD and CFO estimation.

Motivated by these facts, we develop in this paper a new decentralised maximum likelihood (ML) synchronization technique along with a distributed MIMO-relay beamforming design that tackles the challenging TVC case over multi-node relaying transmissions. The proposed ML TVC solution builds upon a very useful approximation of the channel covariance matrix by a two-ray propagation model. It provides accurate ML estimates of the TDs and CFOs at a reduced computational cost because it does not require any matrix inversion. We also develop an iterative version, referred to as ML TVC-DE (Doppler estimate), that accounts for the practical need to estimate at each relay node the Doppler spread upon which relies

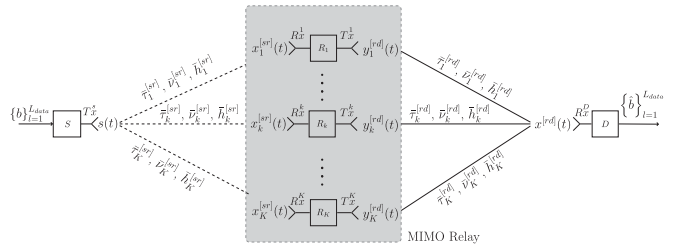


Fig. 1. System model for the distributed MIMO-relay beamforming scheme illustrated during the DT (data transmission) cycles.

the initial version referred to hereafter as ML TVC-PD (perfect Doppler). Simulation results show significant synchronization accuracy improvement over previous distributed multi-node synchronization techniques assuming TCCs. The latter translates into noticeable gains in terms of useful (i.e., after accounting for incurred overhead) link-level throughput, more so at higher Doppler or with more distributed MIMO-relay beamforming nodes.

The rest of the paper is organized as follows. In Section II, we introduce the system model. In Section III, we derive the new ML solution of the underlying estimation problem. The pre-compensation procedure and its corresponding distributed MIMO-relay design are presented in Section IV. In Section V, we run exhaustive computer simulations to assess the performance of the proposed distributed synchronization and MIMO-relay beamforming solution both at the component and link levels in terms of estimation accuracy and throughput, respectively. Finally, we draw out some concluding remarks in Section VI.

The notations adopted in this paper are as follows. Vectors and matrices are represented in lower- and upper-case bold fonts, respectively. The shorthand notation $x \sim \mathcal{CN}(m, \sigma^2)$ denotes a complex normal (i.e., Gaussian) distribution with mean m and variance σ^2 . Moreover, $\{\cdot\}^T$ and $\{\cdot\}^H$ denote the conjugate and Hermitian (i.e., transpose conjugate) operators and $\det\{\cdot\}$ returns the determinant of any square matrix. The Euclidean norm of any vector is denoted as $\|\cdot\|$ and \mathbf{I}_N denotes the $(N \times N)$ identity matrix. For any vector \mathbf{x} , $\text{diag}\{\mathbf{x}\}$ refers to the diagonal matrix whose elements are those of \mathbf{x} . For any matrix \mathbf{X} , $[\mathbf{X}]_q$ and $[\mathbf{X}]_{l,k}$ denote its q^{th} column and $(l, k)^{\text{th}}$ entry, respectively. The element-wise product between any two vectors \mathbf{x}_1 and \mathbf{x}_2 is denoted as $\mathbf{x}_1 \odot \mathbf{x}_2$. Moreover, $\{\cdot\}^*$, $\angle\{\cdot\}$, and $|\cdot|$ return the conjugate, angle, and modulus of any complex number, respectively. Finally, $\mathbb{E}\{\cdot\}$ stands for the statistical expectation, j is the imaginary unit (i.e., $j^2 = -1$), and the notation \triangleq is used for definitions.

II. SYSTEM MODEL

Consider a cooperative decode-and-forward (DF) communication system with a source, S , a destination, D , and a MIMO relay of K randomly distributed nodes, R_1, R_2, \dots, R_K , as shown in Fig. 1. The K relays are subject to CFOs and TDs due to the presence of different local oscillators. We denote the CFOs of the K relays by $(\bar{\nu}_1, \bar{\nu}_2, \dots, \bar{\nu}_K) \subset [0, \nu_{\max}]^K$ and their respective TDs by $(\bar{\tau}_1, \bar{\tau}_2, \dots, \bar{\tau}_K) \subset [0, \tau_{\max}]^K$.

The parameters, ν_{\max} and τ_{\max} , can be set as large as desired within the vicinity of practical CFO and TD values. The true unknown parameters will also carry the superscripts $(\cdot)^{[sr]}$ and $(\cdot)^{[rd]}$ to indicate the communication link to which they belong, i.e., S to R_k and R_k to D , respectively. Most importantly, in stark contrast to previous works on multi-node synchronization which have only dealt so far with TCCs, all the nodes and/or the destination are assumed in this work to be mobile, possibly with different velocities. Hence the second-hop's communication link between each relay node R_k and the destination has a TVC characterized by the Doppler spread σ_{D_k} .

During an initial synchronization period, the final destination starts by broadcasting a common training sequence of L symbols, $\mathbf{a}^{[dr]} \triangleq [a^{[dr]}[1], a^{[dr]}[2], \dots, a^{[dr]}[L]]^T$, to all the relays. Hence, every relay node will be able to estimate its own synchronization parameters locally and independently of all others. This approach, in contrast to [4], alleviates the hurdles of estimating closely-spaced TDs and/or CFOs when implemented jointly at the destination. During this pilot transmission (PT) period, the destination broadcasts the following known signal to all the relays:

$$s^{[dr]}(t) = \sum_{l=0}^{L-1} \mathbf{a}^{[dr]}[l+1]g(t-lT), \quad (1)$$

where $g(t)$ is the pulse-shaping function and T is the symbol duration. The continuous-time received signal at the k^{th} relay is given by:

$$x_k^{[dr]}(t) = h_k^{[dr]}(t)s^{[dr]}(t - \bar{\tau}_k^{[dr]}) e^{j2\pi \bar{\nu}_k^{[dr]}t} + n_k^{[dr]}(t), \quad (2)$$

where $h_k^{[dr]}(t)$ is a flat-fading Rayleigh channel and $n_k^{[dr]}(t)$ is the additive Gaussian noise component assumed to be temporally white. Using its received signal in (2), each relay will find the estimates, $\hat{\tau}_k^{[dr]}$ and $\hat{\nu}_k^{[dr]}$, for its channel TD and CFO, $\bar{\tau}_k^{[dr]}$ and $\bar{\nu}_k^{[dr]}$, respectively. The signal in (2) is oversampled by a factor $Q = T/T_s$ where T_s is the sampling period. The observation sequence corresponding to the sampling time instants, $\{nT_s\}_{n=0}^{QL-1}$, is given by:

$$x_k^{[dr]}(n) = h_k^{[dr]}(n) \sum_{l=0}^{L-1} \mathbf{a}^{[dr]}[l+1]g(nT_s - lT - \bar{\tau}_k^{[dr]}) \times e^{j2\pi \bar{\nu}_k^{[dr]} \frac{nT_s}{Q}} + n_k^{[dr]}(n), \quad (3)$$

where the additive white Gaussian noise is denoted by $n_k^{[dr]}(n) \sim \mathcal{CN}(0, \sigma_{n_k}^2)$. Notice in (3) that we keep using the same notation, $\bar{\nu}_k^{[dr]}$, as in (2) for the normalized (by T_s) CFO between R_k and D , that is for the sake of simplicity.

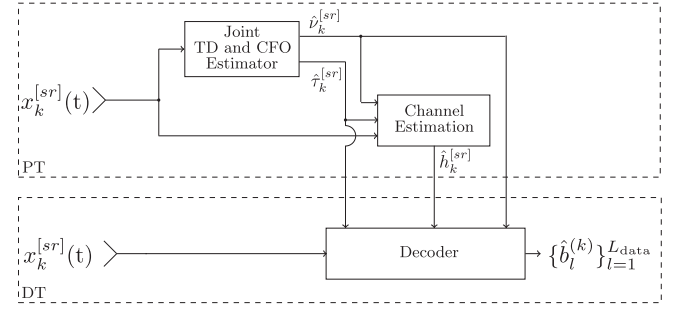


Fig. 2. Block diagram of the DF receiver at the k^{th} relay.

In order to rewrite (3) in a matrix/vector form, we denote by $\mathbf{x}_k^{[dr]} \triangleq [x_k^{[dr]}(0), x_k^{[dr]}(1), \dots, x_k^{[dr]}(QL-1)]^T$, $\mathbf{h}_k^{[dr]} \triangleq [h_k^{[dr]}(0), h_k^{[dr]}(1), \dots, h_k^{[dr]}(QL-1)]^T$, and $\mathbf{n}_k^{[dr]} \triangleq [n_k^{[dr]}(0), n_k^{[dr]}(1), \dots, n_k^{[dr]}(QL-1)]^T$ the vectors that contain, respectively, the received samples, the channel coefficients, and the noise components. We also introduce the following matrix that is parametrized by the generic TD variable τ , $\mathbf{G}(\tau)$, shown at the bottom of this page.

Starting from (3) and resorting to some straightforward algebraic manipulations, it can be shown for $k = 1, 2, \dots, K$ that we have:

$$\mathbf{x}_k^{[dr]} = \mathbf{\Lambda}(\bar{\nu}_k^{[dr]}) \mathbf{\Omega}(\bar{\tau}_k^{[dr]}) \mathbf{h}_k^{[dr]} + \mathbf{n}_k^{[dr]}, \quad (4)$$

where:

$$\mathbf{\Omega}(\tau) \triangleq \text{diag}\{\mathbf{G}(\tau) \mathbf{a}^{[dr]}\}, \quad (5)$$

$$\mathbf{\Lambda}(\nu) \triangleq \begin{pmatrix} 1 & 0 & \dots & 0 \\ 0 & e^{j2\pi\nu} & 0 & \dots & 0 \\ \vdots & \vdots & \vdots & \vdots & \vdots \\ 0 & \dots & \dots & \dots & e^{j2\pi\nu(Q-1)/Q} \end{pmatrix}. \quad (6)$$

For the sake of clarity, we will only focus on the second hop and assume the first hop's estimation and transmission tasks to be ideal. Indeed, as shown in Fig. 2, the proposed synchronization algorithm can also be applied at each relay node to obtain the matched filtered samples required to decode the data locally during the data transmission (DT) period. As such, we will drop in (4) and in all the equations of the next section the $[dr]$ superscript thereby leading to:

$$\mathbf{x}_k = \mathbf{\Lambda}(\bar{\nu}_k) \mathbf{\Omega}(\bar{\tau}_k) \mathbf{h}_k + \mathbf{n}_k. \quad (7)$$

Yet for the sake of completeness, the entire processing and data signaling structure of the two-hop MIMO-relay beamforming scheme is fully illustrated in Fig. 4. And its active building blocks, over the second hop, will be discussed and clarified one by one in the following sections.

$$\mathbf{G}(\tau) \triangleq \begin{pmatrix} g(0-T-\tau) & \dots & g(0-LT-\tau) \\ g(T_s-T-\tau) & \dots & g(T_s-LT-\tau) \\ \vdots & \vdots & \vdots \\ g((QL-1)T_s-T-\tau) & \dots & g((QL-1)T_s-LT-\tau) \end{pmatrix}.$$

III. JOINT TD AND CFO ML ESTIMATOR

A. TCC Case

Under the assumption of static channels, all nodes are stationary and as such the Doppler spread is equal to zero. In this case, the system model in (7) reduces to:

$$\mathbf{x}_k = h_k \mathbf{\Lambda}(\bar{\nu}_k) \mathbf{G}(\bar{\tau}_k) \mathbf{a} + \mathbf{n}_k, \quad (8)$$

where h_k is the channel gain of the communication link between D and R_k . It can be shown that the log-likelihood function (LLF) can be expressed as follows:

$$\mathcal{L}(\nu_k, \tau_k, h_k, \sigma_{n_k}^2) = -\frac{1}{\sigma_{n_k}^2} \|\mathbf{x}_k - h_k \mathbf{\Psi}(\nu_k, \tau_k) \mathbf{a}\|^2 - QL \ln(\pi \sigma_{n_k}^2), \quad (9)$$

where

$$\mathbf{\Psi}(\nu_k, \tau_k) = \mathbf{\Lambda}(\nu_k) \mathbf{G}(\tau_k). \quad (10)$$

First, we maximize $\mathcal{L}(\nu, \tau, h, \sigma_{n_k}^2)$ with respect to the noise variance. The partial derivative of (9) with respect to $\sigma_{n_k}^2$ is given by:

$$\frac{\partial}{\partial \sigma_{n_k}^2} \mathcal{L}(\nu_k, \tau_k, h_k, \sigma_{n_k}^2) = \frac{1}{\sigma_{n_k}^4} \|\mathbf{x}_k - h_k \mathbf{\Psi}(\nu_k, \tau_k) \mathbf{a}\|^2 - \frac{QL}{\sigma_{n_k}^2}.$$

Setting this result to zero and solving for $\sigma_{n_k}^2$ yields the ML estimate for the noise variance:

$$\widehat{\sigma}_{n_k, \text{ML}}^2 = \frac{1}{QL} \|\mathbf{x}_k - h_k \mathbf{\Psi}(\nu_k, \tau_k) \mathbf{a}\|^2, \quad (11)$$

which is substituted back in (9) to obtain the following ML estimates for the remaining parameters at each relay node:

$$[\widehat{\nu}_k, \widehat{\tau}_k, \widehat{h}_k] = \underset{\nu, \tau, h}{\operatorname{argmin}} \mathcal{L}(\nu, \tau, h), \quad (12)$$

where:

$$\mathcal{L}(\nu, \tau, h) = \|\mathbf{x}_k - h \mathbf{\Psi}(\nu, \tau) \mathbf{a}\|^2. \quad (13)$$

For any given couple of values for ν and τ , the LLF optimization over h_k reduces to a linear least squares (LS) problem whose solution is given by:

$$\widehat{h}_k = \frac{1}{\|\mathbf{\Psi}(\nu, \tau) \mathbf{a}\|^2} \mathbf{a}^H \mathbf{\Psi}(\nu, \tau)^H \mathbf{x}_k. \quad (14)$$

By substituting \widehat{h}_k for h_k back in (13) and after some algebraic manipulations, we obtain the so-called *compressed* LLF (CLLF) which depends solely on ν and τ :

$$\begin{aligned} \mathcal{L}_c(\nu, \tau) &= \frac{1}{\|\mathbf{\Psi}(\nu, \tau) \mathbf{a}\|^2} \mathbf{x}_k^H \mathbf{\Psi}(\nu, \tau) \mathbf{a} \mathbf{a}^H \mathbf{\Psi}(\nu, \tau)^H \mathbf{x}_k \\ &= \frac{1}{\|\mathbf{\Psi}(\nu, \tau) \mathbf{a}\|^2} \left[\mathbf{a}^H \mathbf{\Psi}^H(\nu, \tau) \mathbf{x}_k \right]^H \\ &\quad \times \left[\mathbf{a}^H \mathbf{\Psi}^H(\nu, \tau) \mathbf{x}_k \right]. \end{aligned} \quad (15)$$

Hence, the joint ML estimates of ν_k and τ_k become the solution of the following optimization problem:

$$[\widehat{\nu}_k, \widehat{\tau}_k] = \underset{\nu, \tau}{\operatorname{argmax}} \mathcal{L}_c(\nu, \tau). \quad (16)$$

Moreover, noticing that $\mathbf{a}^H \mathbf{\Psi}^H(\nu, \tau) \mathbf{x}_k$ is a scalar quantity, one can rewrite (15) as follows:

$$\mathcal{L}_c(\nu, \tau) = \frac{1}{\|\mathbf{\Psi}(\nu, \tau) \mathbf{a}\|^2} \left| \mathbf{a}^H \mathbf{G}(\tau)^H \mathbf{\Lambda}^H(\nu) \mathbf{x}_k \right|^2. \quad (17)$$

Now, we define the vector $\mathbf{v}(\tau) = \mathbf{G}(\tau) \mathbf{a}$ whose elements are obtained by linearly convolving the training sequence, \mathbf{a} , with the delayed shaping pulse $g(t - \tau)$ and then sampling the output at time instants $\{mT_s\}_{m=0}^{QL-1}$. Therefore, it follows that:

$$\begin{aligned} \mathcal{L}_c(\nu, \tau) &= \frac{1}{\|\mathbf{d}(\nu, \tau)\|^2} \left| \mathbf{v}(\tau)^H \mathbf{\Lambda}^H(\nu) \mathbf{x}_k \right|^2 \\ &= \frac{1}{\|\mathbf{d}(\nu, \tau)\|^2} \left| \sum_{m=0}^{QL-1} v_\tau^*[m+1] x_k[m+1] \right. \\ &\quad \left. \times e^{-j2\pi \nu m/Q} \right|^2, \end{aligned} \quad (18)$$

where $v_\tau(m)$ is the m^{th} element of the vector $\mathbf{v}(\tau)$. By closely inspecting the expression in (18), we observe that the underlying CLLF can be evaluated at each TD candidate value, and all CFO candidate values using fast Fourier transform (FFT) operation.

B. TVC Case

We start by deriving the LLF that depends on all the unknown parameters observed separately at each relay, i.e., $\nu_k, \tau_k, h_k, \sigma_{n_k}^2$. Since the noise components are assumed to be temporally white and Gaussian distributed, i.e., $\mathbf{n}_k \sim \mathcal{CN}(\mathbf{0}, \sigma_{n_k}^2 \mathbf{I}_{QL})$, each vector \mathbf{x}_k in (7) is also Gaussian distributed. Hence, it can be shown that the *actual* LLF at each relay R_k is given by¹:

$$\mathcal{L}(\nu_k, \tau_k, h_k, \sigma_{n_k}^2) = -\ln(\det\{\mathbf{R}_{\mathbf{x}_k \mathbf{x}_k}\}) - \mathbf{x}_k^H \mathbf{R}_{\mathbf{x}_k \mathbf{x}_k}^{-1} \mathbf{x}_k, \quad (19)$$

where $\mathbf{R}_{\mathbf{x}_k \mathbf{x}_k} = \mathbb{E}\{\mathbf{x}_k \mathbf{x}_k^H\}$ is the covariance matrix of the zero-mean observation vector \mathbf{x}_k whose expression follows from (7) as:

$$\mathbf{R}_{\mathbf{x}_k \mathbf{x}_k} = \mathbf{\Lambda}(\nu_k) \mathbf{\Omega}(\tau_k) \mathbf{R}_{\mathbf{h}_k \mathbf{h}_k} \mathbf{\Omega}(\tau_k)^H \mathbf{\Lambda}(\nu_k)^H + \sigma^2 \mathbf{I}_{QL}, \quad (20)$$

where $\mathbf{R}_{\mathbf{h}_k \mathbf{h}_k} = \mathbb{E}\{\mathbf{h}_k \mathbf{h}_k^H\}$. It is obvious that maximizing $\mathcal{L}(\nu_k, \tau_k, h_k, \sigma_{n_k}^2)$ requires the inversion of a large-size ($QL \times QL$) covariance matrix and the computation of its determinant. In the following, we develop a new solution that avoids these costly calculations. Actually, the new solution relies on the two-ray channel approximation² of the covariance matrix of the channel, as described in [24] and [25] (please refer to the Appendix in [24] for more details about the underlying second-order Taylor series approximation), which leads to:

$$\mathbf{R}_{\mathbf{h}_k \mathbf{h}_k} \approx \frac{\sigma_{h_k}^2}{2} \mathbf{W} \mathbf{W}^H, \quad (21)$$

¹After dropping the constant terms.

²It is worth mentioning that the two-ray channel approximation holds only when $LF_{D_k} T \ll 1$.

where $\sigma_{n_k}^2$ is channel variance and \mathbf{W} is defined as follows:

$$\mathbf{W} = [\mathbf{w} \ \mathbf{w}^*]. \quad (22)$$

The vector \mathbf{w} in (22) is given by:

$$\mathbf{w} = \left[1 \ e^{-j\sigma_{D_k} T_s} \ \dots \ e^{-j(Q_L-1)\sigma_{D_k} T_s} \right]^T.$$

Injecting (21) in (20) leads to the following overall covariance matrix approximation:

$$\mathbf{R}_{\mathbf{x}_k \mathbf{x}_k} = \frac{\sigma_{h_k}^2}{2} \mathbf{\Lambda}(\nu_k) \mathbf{C}(\tau_k) \mathbf{C}^H(\tau_k) \mathbf{\Lambda}(\nu_k)^H + \sigma_{n_k}^2 \mathbf{I}_{Q_L}, \quad (23)$$

in which the matrix $\mathbf{C}(\tau_k)$ is defined as follows:

$$\mathbf{C}(\tau_k) \triangleq [\mathbf{c}_1(\tau_k) \ \mathbf{c}_2(\tau_k)] = \mathbf{\Omega}(\tau_k) \mathbf{W}. \quad (24)$$

To find the inverse of $\mathbf{R}_{\mathbf{x}_k \mathbf{x}_k}$ and its determinant, we start by finding the analytical expressions for the eigenvalues of $\mathbf{C}(\tau_k) \mathbf{C}^H(\tau_k)$ and their corresponding eigenvectors. Clearly, the matrix $\mathbf{C}(\tau_k) \mathbf{C}^H(\tau_k)$ is of rank two (cf. Appendix) and has the same non-zero eigenvalues values as $\mathbf{C}^H(\tau_k) \mathbf{C}(\tau_k)$. Since the latter is a 2×2 matrix, its eigenvalues can be computed analytically. Indeed, it can be shown that:

$$\mathbf{C}^H(\tau_k) \mathbf{C}(\tau_k) = \begin{pmatrix} \alpha(\tau_k) & \varphi(\tau_k) \\ \varphi(\tau_k)^* & \alpha(\tau_k) \end{pmatrix}, \quad (25)$$

where:

$$\alpha(\tau_k) = \sum_{n=0}^{Q_L-1} (\Omega_{n,n}(\tau_k))^2, \quad (26)$$

$$\varphi(\tau_k) = \sum_{n=0}^{Q_L-1} (\Omega_{n,n}(\tau_k))^2 e^{2\sigma_{D_k}(n-1)T_s}. \quad (27)$$

From the roots of the characteristic polynomial of the matrix $\mathbf{C}^H(\tau_k) \mathbf{C}(\tau_k)$ in (25), the two eigenvalues are obtained as follows:

$$\lambda_1 = \alpha(\tau_k) + |\varphi(\tau_k)| \quad \text{and} \quad \lambda_2 = \alpha(\tau_k) - |\varphi(\tau_k)|. \quad (28)$$

Hence the corresponding unit-norm eigenvectors are given by:

$$\mathbf{v}_1 = \frac{1}{\sqrt{2}} \begin{bmatrix} \varphi(\tau_k)^* \\ |\varphi(\tau_k)| \end{bmatrix}^T \quad \text{and} \quad \mathbf{v}_2 = \frac{1}{\sqrt{2}} \begin{bmatrix} 1 \\ -\frac{\varphi(\tau_k)^*}{|\varphi(\tau_k)|} \end{bmatrix}^T.$$

Since λ_1 and λ_2 are also the two non-zero eigen-values of $\mathbf{C}(\tau_k) \mathbf{C}^H(\tau_k)$, the singular value decomposition (SVD) of the matrix $\mathbf{C}(\tau_k)$ is obtained as follows:

$$\mathbf{C}(\tau_k) = \mathbf{U}(\tau_k) \mathbf{\Sigma}(\tau_k)^{1/2} \mathbf{V}(\tau_k)^H, \quad (29)$$

where:

$$\mathbf{\Sigma}(\tau_k) \triangleq \text{diag}\{\lambda_1, \lambda_2\} \quad \text{and} \quad \mathbf{V}(\tau_k) \triangleq [\mathbf{v}_1 \ \mathbf{v}_2]. \quad (30)$$

Moreover, since $\mathbf{V}(\tau_k)^H \mathbf{V}(\tau_k) = \mathbf{I}_2$, then $\mathbf{U}(\tau_k) = [\mathbf{u}_1 \ \mathbf{u}_2]$ can be expressed as follows:

$$\mathbf{U}(\tau_k) = \mathbf{C}(\tau_k) \mathbf{V}(\tau_k)^H \mathbf{\Sigma}(\tau_k)^{-1/2}. \quad (31)$$

Therefore, it follows that:

$$\mathbf{u}_1 = \frac{1}{\sqrt{2\lambda_1}} \left(\mathbf{c}_1(\tau_k) + \frac{\varphi(\tau_k)^*}{|\varphi(\tau_k)|} \right), \quad (32)$$

$$\mathbf{u}_2 = \frac{1}{\sqrt{2\lambda_2}} \left(\mathbf{c}_2(\tau_k) - \frac{\varphi(\tau_k)^*}{|\varphi(\tau_k)|} \right). \quad (33)$$

Now, by injecting (29) back into (23), it follows that:

$$\mathbf{R}_{\mathbf{x}_k \mathbf{x}_k} = \sigma_{n_k}^2 \left(\frac{\rho_k}{2} \mathbf{B}(\nu_k, \tau_k) \mathbf{\Sigma}(\tau_k) \mathbf{B}(\nu_k, \tau_k)^H + \mathbf{I}_{Q_L} \right), \quad (34)$$

where $\mathbf{B}(\nu_k, \tau_k) = \mathbf{\Lambda}(\nu_k) \mathbf{U}(\tau_k)$ and $\rho_k = \sigma_{h_k}^2 / \sigma_{n_k}^2$ is the signal-to-noise ratio (SNR). Using the Woodbury identity [26], the inverse of (34) can be computed analytically as follows:

$$\mathbf{R}_{\mathbf{x}_k \mathbf{x}_k}^{-1} = \frac{1}{\sigma_{n_k}^2} \mathbf{I}_{Q_L} - \frac{1}{\sigma_{n_k}^2} \mathbf{B} \left(\frac{2}{\rho_k} \mathbf{\Sigma}^{-1} + \mathbf{B}^H \mathbf{B} \right)^{-1} \mathbf{B}^H, \quad (35)$$

from which, the matrix and vector arguments have been removed for the sake of simplicity. Next, exploiting the fact that \mathbf{u}_1 and \mathbf{u}_2 are orthogonal with unit norms, the inverse of the covariance matrix in (35) can be written as follows:

$$\mathbf{R}_{\mathbf{x}_k \mathbf{x}_k}^{-1} = \frac{1}{\sigma_{n_k}^2} \mathbf{I}_{Q_L} - \frac{1}{\sigma_{n_k}^2} \mathbf{B}(\nu_k, \tau_k) \mathbf{\Gamma}(\tau_k) \mathbf{B}(\nu_k, \tau_k)^H, \quad (36)$$

where:

$$\mathbf{\Gamma}(\tau_k) = \text{diag} \left\{ \frac{\rho_k \lambda_1}{2 + \rho_k \lambda_1}, \frac{\rho_k \lambda_2}{2 + \rho_k \lambda_2} \right\}. \quad (37)$$

Moreover, from (34), it can be shown that the determinant of $\mathbf{R}_{\mathbf{x}_k \mathbf{x}_k}$ is given by:

$$\det\{\mathbf{R}_{\mathbf{x}_k \mathbf{x}_k}\} = \frac{(\sigma_{n_k}^2)^{Q_L}}{4} (\rho_k \lambda_1 + 2)(\rho_k \lambda_2 + 2). \quad (38)$$

Finally, by injecting (36) and (38) back into (19), the LLF reduces to:

$$\begin{aligned} \mathcal{L}(\nu_k, \tau_k, \sigma_{n_k}^2) &= -\ln((\rho_k \lambda_1 + 2)(\rho_k \lambda_2 + 2)) \\ &\quad + \frac{1}{\sigma_{n_k}^2} \left\| \mathbf{\Gamma}(\tau_k)^{1/2} \mathbf{B}(\nu_k, \tau_k)^H \mathbf{x}_k \right\|^2. \end{aligned} \quad (39)$$

By expanding the norm in (39), the LLF can be expressed as follows:

$$\begin{aligned} \mathcal{L}(\nu_k, \tau_k, \sigma_{n_k}^2) &= -\ln((\rho_k \lambda_1 + 2)(\rho_k \lambda_2 + 2)) \\ &\quad + \frac{1}{\sigma_{n_k}^2} \sum_{i=1}^2 \frac{\rho_k \lambda_i}{2 + \rho_k \lambda_i} \left| \mathbf{u}_i^H \mathbf{\Lambda}(\nu_k)^H \mathbf{x}_k \right|^2, \end{aligned} \quad (40)$$

or alternatively as:

$$\begin{aligned} \mathcal{L}(\nu_k, \tau_k, \sigma_{n_k}^2) &= -\ln((\rho_k \lambda_1 + 2)(\rho_k \lambda_2 + 2)) + \frac{1}{\sigma_{n_k}^2} \\ &\quad \times \sum_{i=1}^2 \frac{\rho_k \lambda_i}{2 + \rho_k \lambda_i} \left| \sum_{m=0}^{Q_L-1} \mathbf{u}_i^*[m+1] \right. \\ &\quad \left. \times e^{-j2\pi\nu\frac{m}{Q}} \mathbf{x}_k[m+1] \right|^2, \end{aligned} \quad (41)$$

and the joint ML estimates of ν_k and τ_k , assuming perfect knowledge of the Doppler spread σ_{D_k} , are obtained as the solution to the following two-dimensional optimization problem:

$$[\hat{\nu}_k, \hat{\tau}_k] = \underset{\nu, \tau}{\text{argmax}} \mathcal{L}(\nu, \tau). \quad (42)$$

Note here that the estimates of the SNR, ρ_k , and the noise variance, $\sigma_{n_k}^2$, are obtained using the same approach adopted

in [24]. Moreover, by closely inspecting the expression in (41), we observe that the underlying cost function can be easily evaluated at each candidate value, τ , and all candidate (normalized) CFO values by taking the FFT of the following vector:

$$\mathbf{z}_i(\tau) = \left[u_i^*[1]x_k[1], u_i^*[2]x_k[2], \dots, u_i^*[QL]x_k[QL] \right]^T. \quad (43)$$

Note as well that the candidate values, $\boldsymbol{\nu} = [\nu_1, \nu_2, \dots, \nu_{N_{\text{FFT}}}]^T$, for the unknown CFO parameter are dictated by the size, N_{FFT} , of the underlying FFT:

$$\nu_n = \frac{n-1}{N_{\text{FFT}}}, \quad n = 1, 2, \dots, N_{\text{FFT}}. \quad (44)$$

A larger N_{FFT} allows a more refined sampling of the CFO grid and, therefore, a more accurate estimation. Hence, we can easily use the FFT algorithm to evaluate the LLF for all candidate CFO values, $\boldsymbol{\nu}$, at any given candidate delay value, $\tau[r]$, as follows:

$$\mathbf{d}_r = -\log((\rho\lambda_1 + 2)(\rho\lambda_2 + 2)) + \frac{1}{\sigma_n^2} \times \sum_{i=1}^2 \frac{\rho\lambda_i}{2 + \rho\lambda_i} \times |\text{FFT}(\mathbf{u}_i \odot \mathbf{x}_k)|^2, \quad r = 1, 2, \dots, N_\tau. \quad (45)$$

Hence, the function in (41) is evaluated for all possible TD and CFO values at each relay. The result is a $N_{\text{FFT}} \times N_\tau$ matrix defined as:

$$\mathbf{D} = [\mathbf{d}_1, \mathbf{d}_2, \dots, \mathbf{d}_{N_\tau}]. \quad (46)$$

Finally the estimates $\hat{\nu}_k$ and $\hat{\tau}_k$ are obtained by fetching the global maximum of the matrix \mathbf{D} .

C. Cramer Rao Lower Bound (CRLB)

In the TVC case, the CLRB was previously derived in [27] for the Doppler spread estimation. In the following, we extend it to joint CFO and TD estimation for performance benchmarking. Recall that the covariance matrix of the received signal is given by:

$$\mathbf{R}_{\mathbf{x}_k \mathbf{x}_k} = \mathbf{\Lambda}(\bar{\nu}_k) \mathbf{\Omega}(\bar{\tau}_k) \mathbf{E} \{ \mathbf{h}_k \mathbf{h}_k^H \} \mathbf{\Omega}(\bar{\tau}_k)^H \mathbf{\Lambda}(\bar{\nu}_k)^H + \bar{\sigma}_{n_k}^2 \mathbf{I}_{QL}. \quad (47)$$

Let $\boldsymbol{\zeta} = [\bar{\tau}_k, \bar{\nu}_k, \bar{\sigma}_{n_k}^2]^T$ be a vector that contains all the parameters of interest, then the $(k, l)^{\text{th}}$ element of the Fisher information matrix (FIM) can be written as follows:

$$[\mathbf{J}(\boldsymbol{\zeta})]_{k,l} = \text{trace} \left[\mathbf{R}_{\mathbf{x}_k \mathbf{x}_k}^{-1} \frac{\partial \mathbf{R}_{\mathbf{x}_k \mathbf{x}_k}}{\partial \boldsymbol{\zeta}_k} \mathbf{R}_{\mathbf{x}_k \mathbf{x}_k}^{-1} \frac{\partial \mathbf{R}_{\mathbf{x}_k \mathbf{x}_k}}{\partial \boldsymbol{\zeta}_l} \right]. \quad (48)$$

The CRLBs for the TD and CFO parameters are obtained by finding the inverse of the FIM in (48) and then taking its first and second diagonal entries, respectively.

Algorithm 1 Joint Estimator for the Doppler, TD, and CFO at Each Relay R_K

Initialization: Estimate $\hat{\tau}_k^{(0)}$ and $\hat{\nu}_k^{(0)}$ using (18)

for $j = 1$ to J **do**

Estimate $\hat{\sigma}_{D_k}^{(j)}$

Estimate $\hat{\tau}_k^{(j)}$ and $\hat{\nu}_k^{(j)}$ using (41)

end for

D. Joint Synchronization and Doppler Spread Estimation

The LLF in (41) depends on both the target TD and CFO, but also on the Doppler spread. The latter was assumed thus far to be perfectly known. However, in real life scenarios, the Doppler spread has to be estimated. To reduce the complexity of the tri-dimensional estimation problem, we use a similar approach to the one proposed in [4] in order to find the minimum of some cost function. This approach allows to separate the Doppler estimation problem from the joint synchronization one. As far as the initialization step is concerned, we opt for the TCC technique developed in Subsection III-A to get initial TD and CFO estimates, i.e., $\hat{\tau}_k^{(0)}$ and $\hat{\nu}_k^{(0)}$. The latter are then injected into the LLF of (41) to obtain an initial Doppler spread estimate. This preliminary guess is in its turn injected in the very same LLF function to jointly estimate the TD and CFO. The TCC-based technique is suitable for initialization since it provides good initial estimates for the TVC-based technique. Hence, the latter converges quickly, in few iterations only. The overall estimation technique at each relay R_k is summarized in Algorithm 1. Note that the Doppler estimates can be obtained using (41) after injecting the $\hat{\tau}_k^{(j-1)}$ and $\hat{\nu}_k^{(j-1)}$. Unfortunately, at high Doppler values, the TCC CFO estimates may not be reliable and could affect the performance of the overall algorithm. In such a scenario, we can adopt the technique proposed in [24] which is robust to the CFO and, hence, provides accurate Doppler estimates for injection into the next processing iteration.

IV. DISTRIBUTED MIMO-RELAY BEAMFORMING

Very often, the synchronization process is performed at the destination where the receiver extracts the estimates of all the parameters. This approach could perform well in practice. However, it can suffer from prohibitive computational costs since it requires solving a multi-dimensional problem with a cardinality increasing with the number of relaying nodes [28]. Many techniques opt for sub-optimal iterative implementations [4], [29] that could become ineffective in the case of dense networks. In such a case, open-loop synchronization architectures should be adopted instead. Accordingly, the proposed synchronization technique is run at each relay node along with the distributed MIMO-relay beamforming transceiver structure illustrated in Fig. 3. During a PT period, each node performs a channel parameter estimation task. During the DT period, each relay will transmit the useful data to the destination while ensuring that the signal is modified properly using the TD, CFO and channel estimates made available during the

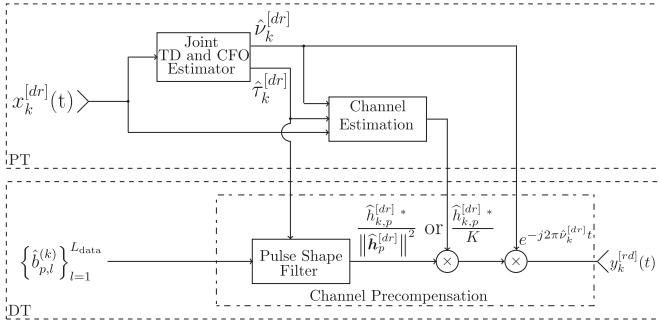


Fig. 3. Block diagram of the DF transceiver at the k^{th} relay.

PT period. Full details of the processing and data signaling structure are shown in Fig. 4. Note that the synchronization parameters are expected to vary with time, but actually at a rate much slower than the channel time-variations. Therefore, as shown in Fig. 4, the synchronization parameters will be refreshed once each P consecutive DT periods.

For more details about the proposed communication protocol, we provide an example on how the processing time and data signaling are organized in the time domain. In fact, during the first period, i.e., step (1), the destination broadcasts a training sequence, $\{a_l^{[rd]}\}_{l=1}^{L_{\text{sync}}}$, to all K relaying nodes. Then, the source node starts transmitting its own training sequence, $\{a_l^{[sr]}\}_{l=1}^{L_{\text{sync}}}$, to the relaying nodes during steps (2) and (3). Each relay node estimates the channel parameters $(\hat{\tau}_k^{[rd]}, \hat{\nu}_k^{[rd]})$ and $(\hat{\tau}_k^{[sr]}, \hat{\nu}_k^{[sr]})$ during steps (4) and (5), respectively. At steps (6) and (7), the destination node broadcasts another training sequence, $\{a_l^{[rd]}\}_{l=1}^{L_{\text{ch}}}$, dedicated to channel estimation. At the same time, the source node performs the same procedure by sending the sequence $\{b_{p,l}\}_{l=1}^{L_{\text{data}}}$ during steps (8) and (9). At step (10), each relay node uses $\hat{\tau}_k^{[sr]}$ and $\hat{\nu}_k^{[sr]}$ along with $\hat{h}_{k,p}^{[sr]}$ to estimate $\{b_{p,l}^{(k)}\}_{l=1}^{L_{\text{data}}}$. The latter will be used along with $\hat{\tau}_k^{[rd]}, \hat{\nu}_k^{[rd]}$, and $\hat{h}_{k,p}^{[rd]}$ to generate the transmitted signal $y_k^{[rd]}(t)$ as described in (53). The signal $y_k^{[rd]}(t)$ is transmitted during step (11). Finally, the destination node performs a simple decoding procedure during step (12). During the next $P-1$ periods (i.e., $1 < p < P$), steps (1) to (5) are ignored since the channel parameters $(\hat{\tau}_k^{[rd]}, \hat{\nu}_k^{[rd]})$ and $(\hat{\tau}_k^{[sr]}, \hat{\nu}_k^{[sr]})$ are assumed to be the same over P periods. At the P^{th} period, however, we execute the same steps (6) to (11) but slightly change the final step (12) and, hence, denote it as (12'). In step (12'), once the destination node completes the decoding process, it starts broadcasting again the very same training sequence $\{a_l^{[rd]}\}_{l=1}^{L_{\text{sync}}}$.

Now, as explained above, the destination periodically transmits to all the relays, at each p^{th} period, a training sequence \mathbf{a}_p that only contains L_{ch} pilot symbols, i.e., $\mathbf{a}^{[dr]} = \{a_l^{[dr]}\}_{l=1}^{L_{\text{ch}}}$. The latter are exploited by each relay to update its channel state information (CSI) with respect to the destination. More specifically, the corresponding oversampled signal

denoted³ here as $\tilde{\mathbf{x}}_k^{[dr]}$ is processed by relay R_k to find the ML estimate of its own complex-valued channel coefficient of the D -to- R_k link during the $\{p^{\text{th}}\}_{p=1}^P$ period, as follows :

$$\hat{h}_{k,p}^{[dr]} = \frac{1}{\|\mathbf{r}(\hat{\nu}_k, \hat{\tau}_k)\|^2} \mathbf{r}^H(\hat{\nu}_k, \hat{\tau}_k) \tilde{\mathbf{x}}_k^{[dr]}, \quad k = 1, 2, \dots, K, \quad (49)$$

where:

$$\mathbf{r}(\nu, \tau) = \mathbf{\Lambda}(\nu) \mathbf{G}(\tau) \mathbf{a}^{[dr]}. \quad (50)$$

To ensure that the signals from all the relays arrive at the receiver coherently and thus combine constructively, the relays must adjust their carrier frequencies, carrier phases, and symbol timings as follows:

- The signal carrying the useful data to be transmitted by the k^{th} relay is delayed as follows:

$$s(t - \hat{\tau}_k^{(\text{comp})}) = \sum_{l=0}^{L_{\text{data}}-1} b_{p,l+1} g(t - lT - \hat{\tau}_k^{(\text{comp})}), \quad (51)$$

where $\{b_{p,l}\}_{l=1}^{L_{\text{data}}}$ are the symbols containing the useful data during the p^{th} period assuming here perfect transmission links between the source and the relays, and $\hat{\tau}_k^{(\text{comp})} = \tau_{\text{max}} - \hat{\tau}_k^{[dr]}$.

- The relay node pre-compensates its CFO by de-rotating the signal in (51) as follows:

$$e^{-j2\pi\hat{\nu}_k^{[dr]}t} s(t - \hat{\tau}_k^{(\text{comp})}). \quad (52)$$

- By relying on the channel reciprocity property of time-division duplex (TDD) schemes, we pre-compensate the channel phase and match its amplitude with the complex channel estimate to generate the following transmit signal $y_k(t)$ at each relay:

$$y_k(t) = \frac{\hat{h}_{k,p}^{[dr]*}}{\|\hat{\mathbf{h}}_p^{[dr]}\|^2} e^{-j2\pi\hat{\nu}_k t} s(t - \hat{\tau}_k^{(\text{comp})}), \quad (53)$$

where $\hat{h}_{k,p}^{[dr]}$ is the channel estimate at the k^{th} relay obtained from (49) and $\hat{\mathbf{h}}_p^{[dr]} = [\hat{h}_{1,p}^{[dr]}, \hat{h}_{2,p}^{[dr]}, \dots, \hat{h}_{K,p}^{[dr]}]^T$. In (53), we need to have the channel estimates over all $D-R$ links available at each relay node for the sole purpose of calculating the square norm of the K -dimensional $D-R$ vector channel. The latter can be fed back by the destination. Alternatively, to avoid any additional overhead, it can be simply approximated by its average value K as follows:

$$y_k(t) \approx \frac{\hat{h}_{k,p}^{[dr]*}}{K} e^{-j2\pi\hat{\nu}_k t} s(t - \hat{\tau}_k^{(\text{comp})}). \quad (54)$$

At the destination, the received signal, $x_p^{[rd]}(t)$, which is the superposition of all the pre-synchronized signals transmitted by the K relays, can be expressed as follows:

$$x_p^{[rd]}(t) = \sum_{k=1}^K \hat{h}_{k,p}^{[rd]}(t) e^{-j2\pi\nu_k t} y_k(t - \tau_k) + w(t), \quad (55)$$

³Note here that $\tilde{\mathbf{x}}_k^{[dr]}$ is equivalent to $\mathbf{x}_k^{[dr]}$ in (7) using, however, another training sequence transmitted specifically for channel estimation purposes.

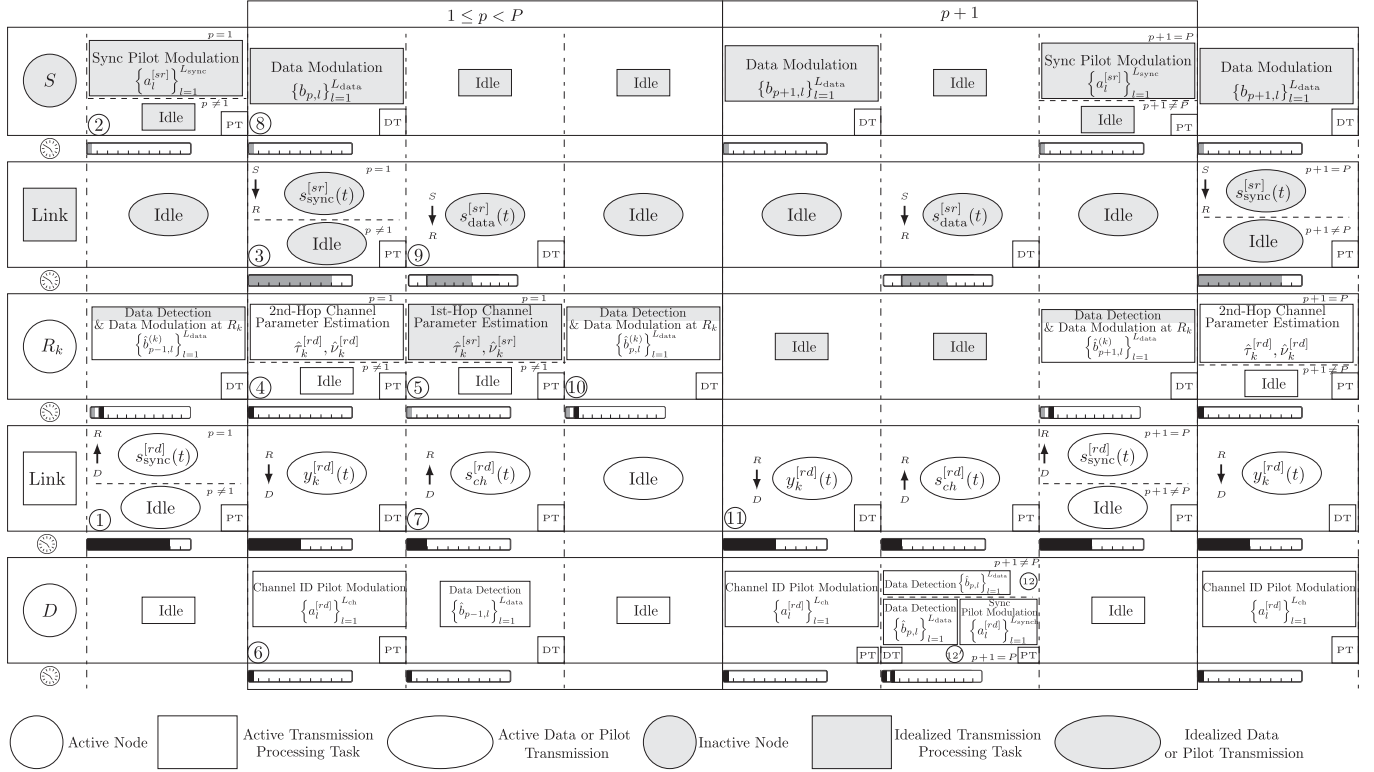


Fig. 4. Processing and data signaling structure of the two-hop MIMO-relay beamforming scheme assuming ideal (inactive) first-hop communication.

where $h_{k,p}^{[rd]}(t)$ is the true TVC pertaining to the k^{th} relay and $w(t)$ is the additive Gaussian noise component received at the destination node. By substituting $y_k(t)$ in (55) with its expression in (53), the received signal stemming from our decentralized multi-node synchronization scheme and distributed MIMO-relay beamforming design is rewritten as follows:

$$x_p^{[rd]}(t) = \sum_{k=1}^K h_{k,p}^{[rd]}(t) \frac{\hat{h}_{k,p}^{[dr]} *}{\|\hat{h}_p^{[dr]}\|^2} e^{j2\pi(\hat{\nu}_k^{[dr]} - \nu_k^{[dr]})t} \times s(t - \hat{\tau}_k^{(\text{comp})} - \tau_k^{[dr]}). \quad (56)$$

V. SIMULATION RESULTS

In the following, we discuss our simulation results at both the component and link levels when all previous works would stop short from moving to the more time consuming yet much more insightful link level. In all our simulations, we assume as would be expected in practice that the K relays are co-located at about the same distance and moving at the same relative speed from the destination whether the latter is stationary or also in motion itself. Under this assumption, the average SNR and the Doppler frequency are assumed to be the same over all R-D and D-R links. Please note that only in the simulations section did we make the choice of considering the simple case of nearly equal SNR and Doppler values over all second-hop channels that could arise in practice in the case for instance of co-located nodes. We did so only for the sake of simplifying our presentation and discussion of the simulation results. Nevertheless, our solution was designed

to cope well with the general case where both the SNR and Doppler frequency values could be different from one second-hop link to another. Beyond the above considerations, co-location could become a required feature among collaborating nodes. For example, it was shown in [30], that multi-hop transmission with co-located cooperating nodes exhibits better coverage especially for higher path loss exponents. Moreover, we know that sensors usually have limited-capacity batteries. And one way to extend their life and allow longer network operation without human intervention is by exploiting wireless energy harvesting (WEH) [31]. Such a solution requires that the sensors be co-located and clustered. In the following, we will investigate in different scenarios the estimation accuracy of the tested synchronization parameter estimators in terms of the normalized mean square error (NMSE) before assessing their link-level throughput performance.

A. Component-Level Simulations

In all component-level simulations, we consider a training sequence, $\mathbf{a}^{[dr]}$, of $L_{\text{sync}} = 128$ QPSK symbols and a square root raised-cosine shaping-pulse filter (SRRC) with a roll-off factor $\rho = 0.3$. In Fig. 5, we compare the proposed technique under its two variants with idealized and active Doppler frequency estimation, i.e., ML TVC-PD and ML TVC-DE, against the space alternating generalized expectation maximization (SAGE) algorithm in [4], the sole benchmark available in the literature dealing with multi-node TD and CFO synchronization, and the CRLBs derived in Section III.B in terms of NMSE performance. We observe that all tested

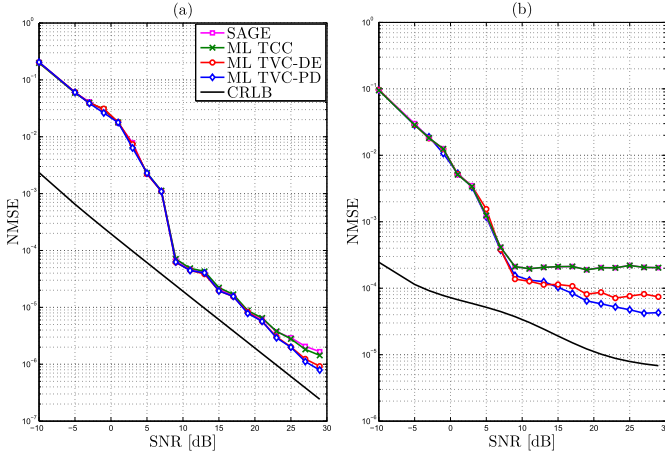


Fig. 5. CRLB and NMSE vs SNR of the ML TVC, ML TCC, and SAGE techniques vs the SNR with $F_{D_k} = 15$ Hz and *uniform Jakes'* model for: (a) the TDs and (b) the CFOs.

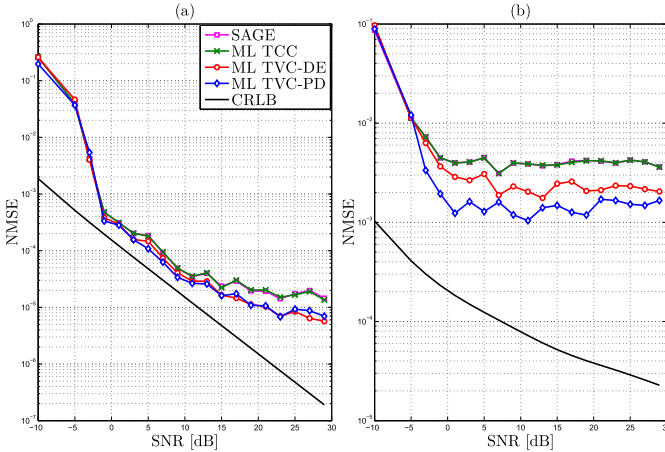


Fig. 6. CRLB and NMSE vs SNR of the ML TVC, ML TCC, and SAGE techniques vs the SNR with $F_{D_k} = 100$ Hz and *uniform Jakes'* model for: (a) the TDs and (b) the CFOs.

techniques perform nearly the same at $F_{D_k} = 15$ Hz with a small advantage for both TVC-PD and TVC-DE measured at high SNR values. On the other hand, SAGE and ML TCC - which perform exactly the same because they both rely on the TCC assumption - see their performance slightly degrade at high SNR because the channel is not totally constant (i.e., $F_{D_k} \neq 0$ Hz). Besides, we observe that the practical ML TVC-DE version matches its idealized ML TVC-PD counterpart in terms of TD estimation accuracy whereas it exhibits slightly lower CFO estimation performance. In fact, this degradation stems from the Doppler estimation errors that increase at higher Doppler values with an even more detrimental impact on CFO estimation.

In Fig. 6, we tackle a more challenging case with a significantly higher Doppler frequency $F_{D_k} = 100$ Hz. Here again, we can report the very same qualitative observations made in Fig. 5, yet with more prominent performance gaps this time in terms of CFO and TD estimation accuracies, more so at high SNR values, between on one hand ML TVC and the TCC-based techniques (i.e., SAGE and ML TCC) and on the other hand between ML TVC-PD and ML TVC-DE.

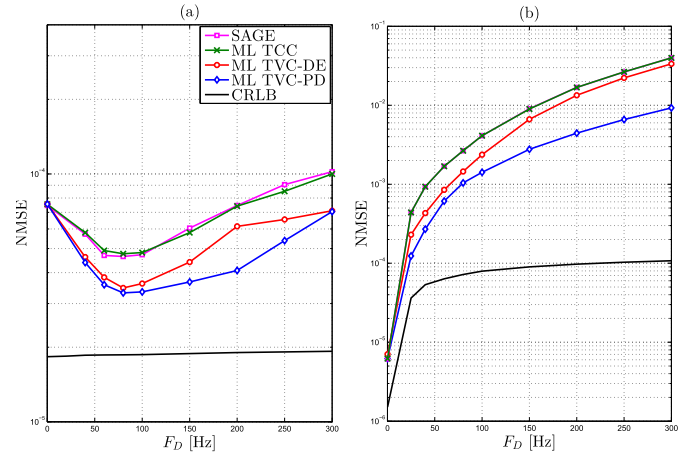


Fig. 7. CRLB and NMSE vs F_{D_k} of the ML TVC, ML TCC, and SAGE techniques with $SNR = 10$ dB and *uniform Jakes'* model for: (a) the TDs, and (b) the CFOs.

This is hardly surprising because on one hand SAGE and ML TCC fail to reach the global maximum and exhibit poor performance since the TCC assumption no longer holds at high Doppler. And because, on the other hand, the Doppler estimator selected for joint operation with the new ML TVC technique to illustrate its applicability in real-world operating conditions is specifically tailored to cope with the far more challenging estimation of low Doppler frequencies. Hence, the additional performance losses resulting from the joint estimation of high Doppler frequencies can be reduced to the same small if not negligible amounts observed at low Doppler in Fig. 5; that is by the simple integration of alternative Doppler estimation solutions easily prone to be made relatively much more accurate at high Doppler.

To better investigate the effect of Doppler frequency on the synchronization accuracy, we plot in Fig. 7 the NMSE of all techniques against the Doppler. Obviously both ML TVC-PD and ML TVC-DE outperform the TCC-based techniques (i.e., SAGE and ML TCC) over a wide Doppler range (i.e., $F_{D_k} \leq 300$ Hz). As the Doppler increases, the TCC-based techniques start experiencing serious difficulties to converge to the global maximum that translate into extremely poor TD and CFO estimation accuracies.

In Fig. 8, we assess the performance variations of the same tested techniques against the training sequence length. We observe that TVC-PD outperforms both ML TCC and SAGE algorithms in terms of CFO estimation accuracy no matter the number of symbols. Recall that both TVC-PD and TVC-DE rely on a two-ray channel approximation (cf. Section III-B) that holds only when $L_{\text{sync}} F_{D_k} T \ll 1$ [24]. Hence, when increasing the training sequence's size at small Doppler values, both techniques see their NMSE performance improve. However, the approximation becomes inaccurate with even longer sequences, more so at higher Doppler, thereby resulting beyond some best trade-off length in counter-effect accuracy losses.

B. Link-Level Simulations

Our link-level simulations were run using the key setup parameters listed in Table I.

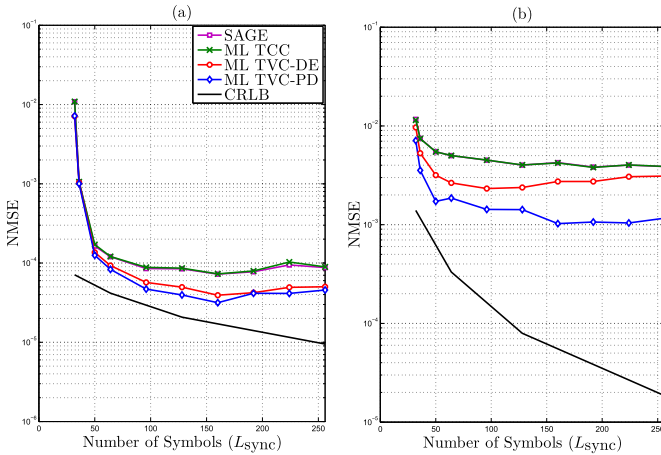


Fig. 8. CRLB and NMSE vs the number of pilot symbols L_{sync} of the ML TVC, ML TCC, and SAGE techniques with $\text{SNR} = 10$ dB, $F_{D_k} = 100$ Hz, and *uniform Jakes'* model for: (a) the TDs, and (b) the CFOs.

TABLE I
SIMULATION PARAMETERS

Parameters	Symbol	Values
Symbol period	T	1/14 ms
Number of relays	K	{1, 2, 4, 8}
Maximum Doppler shift	$\{F_{D_k}\}_{k=1}^K$	{15, 100, 200, 300} Hz
Oversampling factor	Q	2
Roll-off factor	ρ	0.3
TDs	τ_k	Uniformly random (i.i.d.)
CFOs	ν_k	Uniformly random (i.i.d.)
$R_k - D$ channel	\mathbf{h}_k	Rayleigh random (i.i.d.)

Fig. 9 depicts the resulting throughput for three different modulation orders (QPSK, 16-QAM and 64-QAM) and K relays. We consider in Figs. 9 (a) and 9 (b) the case where all K relay-destination links have the same maximum Doppler frequency shift of 15 and 100 Hz, respectively. For a given modulation order M , the throughput is obtained from the symbol error rate (SER) as follows:

$$\text{Throughput} = \frac{1}{T} \log_2(M)(1 - \text{SER})(1 - R), \quad (57)$$

where R is the overhead ratio. Note here that the latter is computed over a period that spans L_{sync} symbols for synchronization and P periods each of which includes $L_{\text{ch}} = 2$ pilot symbols followed by $L_{\text{data}} = 12$ information-bearing symbols. As such, the overhead ratio is given by:

$$R = \frac{L_{\text{sync}} + L_{\text{ch}}P}{L_{\text{sync}} + (L_{\text{ch}} + L_{\text{data}})P}. \quad (58)$$

Our simulations were obtained for $L_{\text{sync}} = 128$ and $P = 100$. Note here that the overhead ratio associated with the synchronization period becomes negligible for such large value of P . The latter cannot, however, be increased indefinitely as it is dictated by the required refreshment rate P that better copes with the time variations of the synchronization parameters.

We see from Fig. 9 (a) that QPSK transmissions, among the different considered modulations, provide higher throughput for SNR values below 11 dB. When the SNR ranges between 11 dB and 16 dB, 16-QAM becomes more suitable whereas 64-QAM dominates when the SNR exceeds 16 dB.

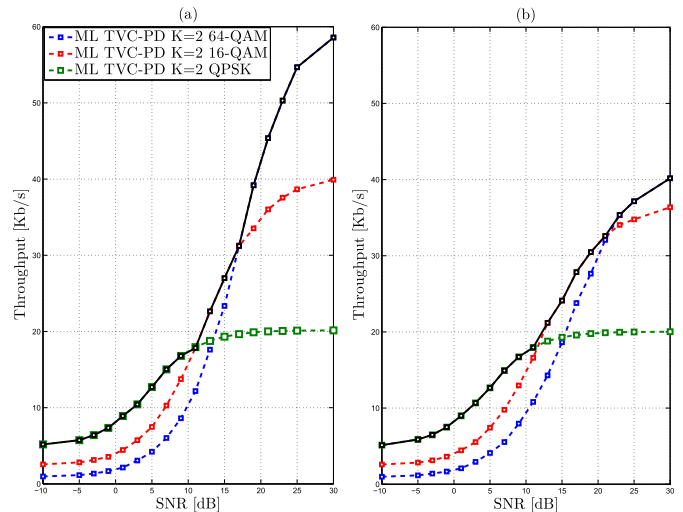


Fig. 9. Link-level throughput vs SNR for ML TVC-PD at $K = 2$ relays and a refreshment rate $P = 100$ for: (a) $\{F_{D_k}\}_{k=1}^K = 15$ Hz, and (b) $\{F_{D_k}\}_{k=1}^K = 100$ Hz.

The resulting throughput curve assuming an adaptive (i.e., SNR-dependent) modulation is depicted by the black curve.

In Fig. 9 (b), we show the performance of the proposed distributed beamforming scheme at a higher Doppler $F_{D_k} = 100$ Hz (i.e., fast TVCs). In this scenario, QPSK and 16-QAM modulations provide higher throughput over the same SNR ranges reported above at low Doppler whereas 64-QAM dominates when the SNR exceeds 21 dB. We also observe that 64-QAM transmissions suffer from a noticeable performance degradation. Indeed, at lower Doppler values, the phase estimates of (49) provide accurate values since the channel varies slowly during the same period. Hence, the decoder at the destination is able to accurately estimate the transmitted symbols. In the case of high mobility, the channel varies rapidly during the same period, leading to a more severe degradation of the channel estimates. The latter affects the decoding process, especially at higher modulations which are more sensitive to phase shifts.

In Fig. 10, we compare the performance of ML TVC-PD and ML TVC-DE in terms of throughput. The former sees its performance deteriorate against the former only at high SNR. Measured losses are almost negligible at low Doppler, but become noticeable at high Doppler. Yet, as reported previously when discussing the component-level simulation results, such link-level throughput gap can be easily bridged by the integration of an alternative high-range Doppler estimator, thereby making ML TVC-PD an equivalent version to ML TVC-DE and a meaningful one for further comparisons in what follows with existing Doppler-independent TCC-based benchmarks.

In Fig. 11, we assess the performance of ML TVC-PD in the more realistic case of an active first-hop scenario, that is to gauge in comparison the usefulness of the results obtained in the idealized case of perfect $D - R$ transmissions. Actually, the impact of active first-hop links is emulated by inserting

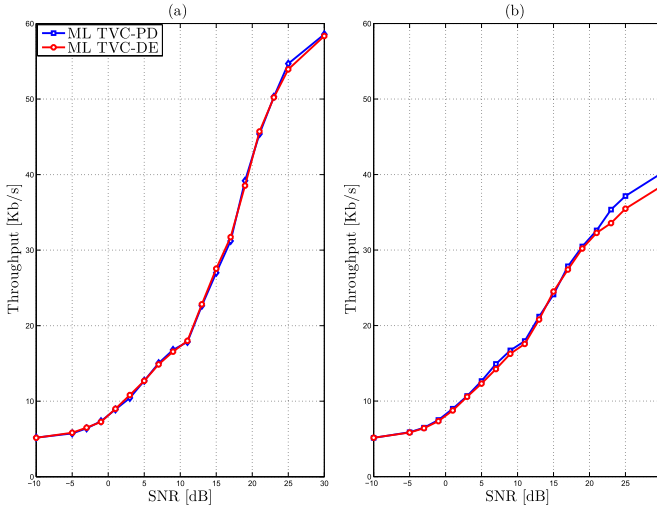


Fig. 10. Link-level throughput vs SNR for ML TVC-PD and ML TVC-DE at $K = 2$ relays, $\{F_{D_k}\}_{k=1}^K = 100$ Hz, and a refreshment rate $P = 100$ for: (a) $\{F_{D_k}\}_{k=1}^K = 15$ Hz, and (b) $\{F_{D_k}\}_{k=1}^K = 100$ Hz.

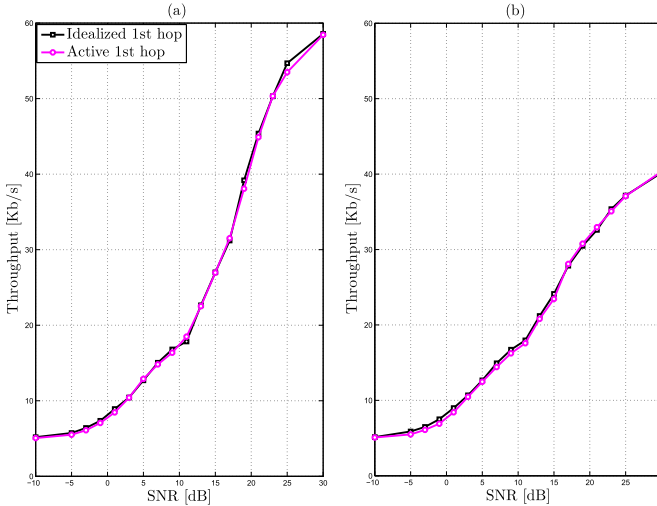


Fig. 11. Link-level throughput vs SNR for ML TVC-PD at $K = 2$ relays and a refreshment rate $P = 100$ for: (a) $\{F_{D_k}\}_{k=1}^K = 15$ Hz, and (b) $\{F_{D_k}\}_{k=1}^K = 100$ Hz.

erroneous symbols at each relay. The latter are generated with a probability resulting from an SNR level 5 dB higher than the one measured at the destination. This is to reflect the fact that relays are expectedly selected at more favorable locations than the destination. We see that the throughput curve of the two-hop scenario exhibits approximately the same performance as the one considering an idealized first-hop communication. Such a result confirms that the throughput of the MIMO-relay beamforming system is mainly dictated by the performance of the relatively weaker-SNR second-hop.

In Fig. 12, we compare the performance of ML TVC-PD, ML TCC, and SAGE in terms of throughput for four different numbers of relays ($K = 1$, $K = 2$, $K = 4$, and $K = 8$) and four different Doppler frequencies (i.e., $\{F_{D_k}\}_{k=1}^K = 15$ Hz, $\{F_{D_k}\}_{k=1}^K = 100$ Hz, $\{F_{D_k}\}_{k=1}^K = 200$ Hz, and $\{F_{D_k}\}_{k=1}^K = 300$ Hz). We see under the TCC assumption

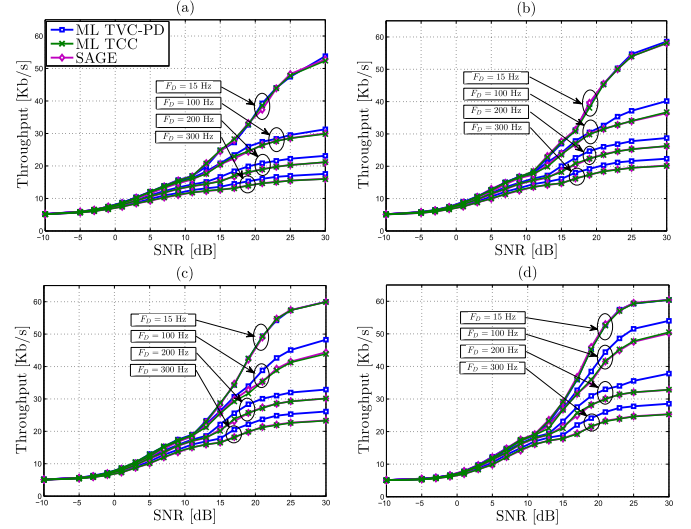


Fig. 12. Link-level throughput vs SNR for ML TVC-PD at a refreshment rate $P = 100$ and different Doppler frequencies for: (a) $K = 1$, (b) $K = 2$, (c) $K = 4$, and (d) $K = 8$.

(i.e., $F_{D_k} = 15$ Hz) that all techniques perform nearly the same in terms of link-level throughput. They do so the best with QPSK transmissions when the SNR is below 11 dB whereas 16-QAM becomes more suitable at SNR values ranging between 11 and 16 dB. When the SNR exceeds 16 dB, 64-QAM transmissions ultimately become the best choice. At a higher Doppler frequency (i.e., $F_{D_k} = 100$ Hz), we can always report noticeable and constantly increasing throughput gains of ML TVC over TCC-based SAGE and ML TCC at both medium and high SNR levels when increasing the number of relays from 1 to 8. At lower SNR values, all techniques exhibit the same NMSE and consequently the same throughput performances. At even higher Doppler values (i.e., $F_{D_k} = 200$ Hz or $F_{D_k} = 300$ Hz), the relative throughput gains of ML TVC over SAGE and ML TCC become even more significant, again more so when the number of relays also increases. These key observations come as a solid confirmation of the very important performance benefits of the proposed distributed MIMO-relay beamforming and multi-node synchronization schemes.

VI. CONCLUSION

In this paper, we addressed the problem of time and frequency synchronization in cooperative systems over TVCs. We proposed two different estimation techniques. The first operates under the TVC assumption while the second one works with TCCs. In the first ML TVC-PD approach, we assume perfect knowledge of the Doppler spread to provide accurate TD and CFO synchronization estimates. Whereas we exploit the second ML TCC technique as an initialization scheme for preliminary synchronization then embed both ML TVC-PD and some Doppler estimator in a new iterative version, ML TVC-DE. That is to account for the practical need to estimate at each relay node the Doppler spread upon which relies ML TVC-PD. We also developed a new distributed MIMO-relay beamforming design that embeds the proposed

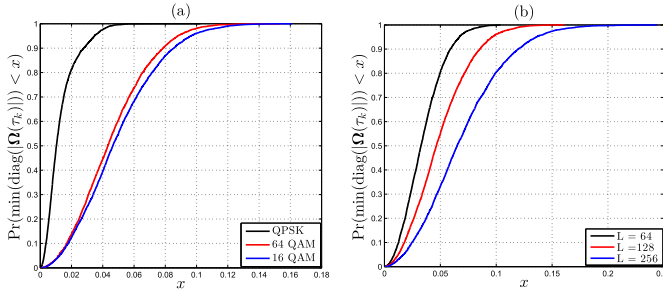


Fig. 13. CDF of the minimum of absolute value of $\text{diag}\{\Omega(\tau_k)\}$ for: (a) multiple modulation orders, and (b) multiple sequence lengths.

synchronization technique at each relay node. We showed under the TCC assumption that all techniques exhibit approximately the same performance. However, when the Doppler increases, the TCC-based techniques exhibit poor performance while the new ML TVC continues to provide accurate estimates. Link-level simulations confirm the net advantages of the proposed ML TVC multi-node synchronization technique and the MIMO-relay beamforming scheme in terms of throughput gains, especially at medium and high SNRs, more so at relatively higher Doppler frequencies or with more distributed MIMO-relay beamforming nodes. Future work could investigate a more complex system that includes multiple antennas at each relay nodes and/or multiple receivers.

APPENDIX

RELATIONSHIP BETWEEN THE RANK OF $\mathbf{C}(\tau_k)\mathbf{C}^H(\tau_k)$ AND THE TWO-RAY APPROXIMATION

As stated in [24], by adopting the two-ray approximation model, the approximate channel covariance matrix, $\hat{\mathbf{R}}_{h_k h_k}$, is of rank two. However, introducing the diagonal matrix $\Omega(\tau_k)$ (i.e., $\mathbf{C}(\tau_k)\mathbf{C}^H(\tau_k) = \Omega(\tau_k)\hat{\mathbf{R}}_{h_k h_k}\Omega(\tau_k)^H$) does not guarantee that $\mathbf{C}(\tau_k)\mathbf{C}^H(\tau_k)$ remains of rank two. To find the rank of $\mathbf{C}(\tau_k)\mathbf{C}^H(\tau_k)$, we start with the following:

$$\begin{aligned} \text{rank}(\mathbf{C}(\tau_k)) &= \text{rank}(\Omega(\tau_k)\mathbf{W}) \\ &\leq \min\{\text{rank}(\Omega(\tau_k)), \text{rank}(\mathbf{W})\}. \end{aligned} \quad (59)$$

We have also:

$$\begin{aligned} \text{rank}(\Omega(\tau_k)) + \text{rank}(\mathbf{W}) - Q L_{\text{sync}} &\leq \text{rank}(\Omega(\tau_k)\mathbf{W}) \\ &= \text{rank}(\mathbf{C}(\tau_k)). \end{aligned} \quad (60)$$

If $\Omega(\tau_k)$ is a full rank matrix, then by using (59) and (60), it follows that:

$$\text{rank}(\mathbf{C}(\tau_k)) = \text{rank}(\mathbf{W}). \quad (61)$$

Since $\Omega(\tau_k)$ is a diagonal matrix, by establishing that $\{\{\Omega(\tau_k)\}_{qq} \neq 0\}_{q=1}^{Q L_{\text{sync}}}$, we can prove that $\Omega(\tau_k)$ is a full rank matrix. Now, recall that:

$$\Omega(\tau) \triangleq \text{diag}\{\mathbf{G}(\tau)\mathbf{a}^{[dr]}\}. \quad (62)$$

Hence, the diagonal elements of $\Omega(\tau)$ are given by:

$$[\Omega(\tau)]_{qq} = \sum_{l=0}^{L_{\text{sync}}} a^{[dr]}[l+1]g(qT_s - L_{\text{sync}}T - \tau), \quad (63)$$

which are always non-zero elements due to the omnipresence in time of ISI components. It follows that $\Omega(\tau)$ is a diagonal matrix with non-zero elements and, hence, full rank. As seen in Fig. 13, the probability that the absolute values of the diagonal element be equal to zeros is zero. Besides, $\mathbf{W} = [\mathbf{w}\ \mathbf{w}^*]$ was proved to be of rank two in [25]. It follows from (61) that $\mathbf{C}(\tau_k)$ is also of rank two. And since for any matrix we have:

$$\begin{aligned} \text{rank}(\mathbf{C}(\tau_k)\mathbf{C}(\tau_k)^H) &= \text{rank}(\mathbf{C}(\tau_k)^H\mathbf{C}(\tau_k)) \\ &= \text{rank}(\mathbf{C}(\tau_k)) = \text{rank}(\mathbf{W}), \end{aligned} \quad (64)$$

we establish that $\mathbf{C}(\tau_k)\mathbf{C}^H(\tau_k)$ is of rank two as well and also prove by the same token that this rank value is entirely related to the two-ray approximation, indeed.

REFERENCES

- [1] S. Ben Amor, S. Affes, F. Bellili, U. Vilaipornsawai, L. Zhang, and P. Zhu, "ML time-delay and CFO synchronization for MIMO-relay beamforming over time-varying channels," in *Proc. IEEE Global Commun. Conf. (GLOBECOM)*, Abu Dhabi, UAE, Dec. 2018, pp. 1–7.
- [2] A. Sendonaris, E. Erkip, and B. Aazhang, "User cooperation diversity. part I. system description," *IEEE Trans. Commun.*, vol. 51, no. 11, pp. 1927–1938, Nov. 2003.
- [3] Y. Jing and H. Jafarkhani, "Network beamforming using relays with perfect channel information," *IEEE Trans. Inf. Theory*, vol. 55, no. 6, pp. 2499–2517, Jun. 2009.
- [4] A. A. Nasir, H. Mehrpouyan, S. D. Blostein, S. Durrani, R. A. Kennedy, and S. D. Blostein, "Timing and carrier synchronization with channel estimation in multi-relay cooperative networks," *IEEE Trans. Signal Process.*, vol. 60, no. 2, pp. 793–811, Feb. 2012.
- [5] H. Wang, X.-G. Xia, and Q. Yin, "Computationally efficient equalization for asynchronous cooperative communications with multiple frequency offsets," *IEEE Trans. Wireless Commun.*, vol. 8, no. 2, pp. 648–655, Feb. 2009.
- [6] Y.-S. Tu and G. J. Pottie, "Coherent cooperative transmission from multiple adjacent antennas to a distant stationary antenna through AWGN channels," in *Proc. 55th Veh. Technol. Conf. (VTC)*, Birmingham, AL, USA, May 2002, pp. 130–134.
- [7] A. A. Nasir, S. Durrani, H. Mehrpouyan, S. D. Blostein, and R. A. Kennedy, "Timing and carrier synchronization in wireless communication systems: A survey and classification of research in the last 5 years," *EURASIP J. Wireless Commun. Netw.*, vol. 2016, p. 180, Dec. 2016.
- [8] X. Li, C. Xing, Y.-C. Wu, and S. C. Chan, "Timing estimation and resynchronization for amplify-and-forward communication systems," *IEEE Trans. Signal Process.*, vol. 58, no. 4, pp. 2218–2229, Apr. 2010.
- [9] H. Mehrpouyan and S. D. Blostein, "Estimation, training, and effect of timing offsets in distributed cooperative networks," in *Proc. IEEE Global Commun. Conf. (GLOBECOM)*, Miami, FL, USA, Dec. 2010, pp. 1–5.
- [10] M. T. Hossain, D. B. Smith, and S. Kandeepan, "Timing synchronization for cooperative communications with detect and forward relaying," *Wireless Pers. Commun.*, vol. 62, no. 2, pp. 363–378, Jan. 2012.
- [11] X. Li, Y. C. Wu, and E. Serpedin, "Timing synchronization in decode-and-forward cooperative communication systems," *IEEE Trans. Signal Process.*, vol. 57, no. 4, pp. 1444–1455, Apr. 2009.
- [12] H. Mehrpouyan and S. D. Blostein, "Bounds and algorithms for multiple frequency offset estimation in cooperative networks," *IEEE Trans. Wireless Commun.*, vol. 10, no. 4, pp. 1300–1311, Apr. 2011.
- [13] J. Xiong, Q. Huang, Y. Xi, D. Ma, and J. Wei, "Multiple carrier frequency offsets tracking in co-operative space-frequency block-coded orthogonal frequency division multiplexing systems," *IET Commun.*, vol. 7, no. 3, pp. 263–269, Feb. 2013.
- [14] T.-H. Pham, A. Nallanathan, and Y.-C. Liang, "Joint channel and frequency offset estimation in distributed MIMO flat-fading channels," *IEEE Trans. Wireless Commun.*, vol. 7, no. 2, pp. 648–656, Feb. 2008.
- [15] J.-H. Lee and S.-C. Kim, "Time and frequency synchronization for OFDMA uplink system using the SAGE algorithm," *IEEE Trans. Wireless Commun.*, vol. 6, no. 4, pp. 1176–1181, Apr. 2007.

- [16] S. Chakraborty and D. Sen, "Joint estimation of time, frequency offsets, and channel gains with ICIs in EF multi-relay DMIMO-OFDM system," *IEEE Trans. Veh. Technol.*, vol. 66, no. 7, pp. 5822–5838, Jul. 2017.
- [17] S. Jayaprakasam, S. K. A. Rahim, and C. Y. Leow, "Distributed and collaborative beamforming in wireless sensor networks: Classifications, trends, and research directions," *IEEE Commun. Surveys Tuts.*, vol. 19, no. 4, pp. 2092–2116, 4th Quart., 2017.
- [18] H. Yang, D. Liu, Y. Fan, C. Qian, Z. Zheng, and B. Yan, "Variable directional perturbation with one-bit feedback for collaborative beamforming," in *Proc. IEEE/CIC Int. Conf. Commun. China (ICCC)*, Jul. 2016, pp. 1–5.
- [19] F. Quitin, M. M. Ur Rahman, R. Mudumbai, and U. Madhow, "Distributed beamforming with software-defined radios: Frequency synchronization and digital feedback," in *Proc. IEEE Global Commun. Conf. (GLOBECOM)*, Anaheim, CA, USA, Dec. 2012, pp. 4787–4792.
- [20] M. A. Alvarez and U. Spagnolini, "Distributed time and carrier frequency synchronization for dense wireless networks," *IEEE Trans. Signal Inf. Process. Over Netw.*, vol. 4, no. 4, pp. 683–696, Dec. 2018.
- [21] R. He *et al.*, "High-speed railway communications: From GSM-R to LTE-R," *IEEE Veh. Technol. Mag.*, vol. 11, no. 3, pp. 49–58, Sep. 2016.
- [22] I. Thibault, G. E. Corazza, and L. Deambrogio, "Phase synchronization algorithms for distributed beamforming with time varying channels in wireless sensor networks," in *Proc. 7th Int. Wireless Commun. Mobile Comput. Conf.*, Jul. 2011, pp. 77–82.
- [23] W. Tushar, D. B. Smith, A. Zhang, T. A. Lamahewa, and T. Abhayapala, "Distributed transmit beamforming: Phase convergence improvement using enhanced one-bit feedback," in *Proc. IEEE Wireless Commun. Netw. Conf. (WCNC)*, Paris, France, Apr. 2012, pp. 528–532.
- [24] M. Souden, S. Affes, J. Benesty, and R. Bahroun, "Robust Doppler spread estimation in the presence of a residual carrier frequency offset," *IEEE Trans. Signal Process.*, vol. 57, no. 10, pp. 4148–4153, Oct. 2009.
- [25] F. Bellili, Y. Selmi, S. Affes, and A. Ghayeb, "A low-cost and robust maximum likelihood joint estimator for the Doppler spread and CFO parameters over flat-fading Rayleigh channels," *IEEE Trans. Commun.*, vol. 65, no. 8, pp. 3467–3478, Aug. 2017.
- [26] K. B. Petersen and M. S. Pedersen, "The matrix cookbook," Tech. Univ. Denmark, Lyngby, Denmark, Tech. Rep. ver. 20121115, Nov. 2012. [Online]. Available: <http://www2.imm.dtu.dk/pubdb/p.php?3274>
- [27] C. Tepedelenlioğlu, "Performance analysis of velocity (Doppler) estimators in mobile communications," in *Proc. IEEE Int. Conf. Acoust., Speech, Signal Process.*, Orlando, FL, USA, May 2002, pp. III-2201–III-2204.
- [28] Y. Tian, X. Lei, Y. Xiao, and S. Li, "ML synchronization algorithm and estimation bounds for cooperative systems," in *Proc. 2nd Pacific-Asia Conf. Circuits, Commun. Syst.*, Beijing, China, Aug. 2010, pp. 379–382.
- [29] Y. Tian, X. Lei, Y. Xiao, and S. Li, "SAGE based joint timing-frequency offsets and channel estimation in distributed MIMO systems," *Comput. Commun.*, vol. 33, no. 17, pp. 2125–2131, Aug. 2010.
- [30] S. A. Hassan and M.-A. Ingram, "The benefit of co-locating groups of nodes in cooperative line networks," *IEEE Commun. Lett.*, vol. 16, no. 2, pp. 234–237, Feb. 2012.
- [31] P. V. Mekikis, A. Antonopoulos, E. Kartsakli, A. S. Lalos, L. Alonso and, C. Verikoukis, "Information exchange in randomly deployed dense WSNs with wireless energy harvesting capabilities," *IEEE Trans. Wireless Commun.*, vol. 15, no. 4, pp. 3008–3018, Apr. 2016.



Souheib Ben Amor was born in Hammam Sousse, Sousse, Tunisia, in 1989. He received the Dipl.Ing. degree in telecommunications from the National Engineering School of Tunis, in 2013, and the M.Sc. degree from the Institut National de la Recherche Scientifique-Énergie, Matériaux, et Télécommunications (INRS-ÉMT), Université du Québec, Montréal, QC, Canada, in 2016.

He held an internship at Ericsson Canada in the winter 2015, as part of the CREATE-PERSWADE training program. He was also a Research Intern at Interdigital Canada in the summer 2015.

He is currently pursuing the Ph.D. degree with INRS-ÉMT. His Ph.D. program is in the field of statistical signal processing and array processing and their applications in wireless communications. He received a scholarship for M.Sc. studies under the agreement between the Tunisian Government and INRS-ÉMT. He also received the INRS Scholarship for his Ph.D. studies.



Sofiene Affes (S'95–SM'05) received the Dipl.Ing. degree in telecommunications, and the Ph.D. degree (Hons.) in signal processing from Télécom ParisTech (ENST), Paris, France, in 1992 and 1995, respectively. He was a Research Associate with INRS, Montreal, QC, Canada, until 1997, an Assistant Professor until 2000, and an Associate Professor until 2009. He is currently a Full Professor and the Director of PERSWADE, a unique \$4M research-training program on wireless in Canada, involving 27 partners from 8 universities and 10 industrial

organizations. He currently serves as a member of the Editorial Board of *Sensors* (MDPI) and the Advisory Board of the multi-disciplinary journal *Sci. (MDPI)*. He has been twice a recipient of the Discovery Accelerator Supplement Award from NSERC, from 2008 to 2011 and from 2013 to 2016. From 2003 to 2013, he was the Canada Research Chair in wireless communications. Since 2017, he has been holding the Cyrille-Duquet Research Chair in Telecommunications. In 2006, 2015, and 2017, he served as the General Co-Chair or Chair of the IEEE VTC'2006-Fall, the IEEE ICUWB'2015, and the IEEE PIMRC'2017, respectively, all held in Montreal, QC, Canada. In 2008 and 2015, he received the IEEE VTC Chair Recognition Award from the IEEE VTS and the IEEE ICUWB Chair Recognition Certificate from the IEEE MTT-S for exemplary contributions to the success of both events, respectively. He previously served as an Associate Editor for the IEEE TRANSACTIONS ON WIRELESS COMMUNICATIONS, the IEEE TRANSACTIONS ON SIGNAL PROCESSING, the IEEE TRANSACTIONS ON COMMUNICATIONS, the *Journal of Electrical and Computer Engineering* (Hindawi), and the *Journal of Wireless Communications and Mobile Computing* (Wiley).



Faouzi Bellili received the B.Eng. degree (Hons.) in electrical engineering from Tunisia Polytechnic School, in 2007, and the M.Sc. and Ph.D. degrees (Hons.) from the National Institute of Scientific Research (INRS), University of Quebec, Montreal, QC, Canada, in 2009 and 2014, respectively. From 2014 to 2016, he was a Research Associate at INRS-EMT, where he coordinated a major multi-institutional NSERC Collaborative R&D (CRD) Project on 5th-Generation (5G) Wireless Access Virtualization Enabling Schemes (5G-WAVES). From

2016 to 2018, he was a Post-Doctoral Fellow at the University of Toronto, ON, Canada. He is currently an Assistant Professor with the Department of Electrical and Computer Engineering, University of Manitoba, Winnipeg, MB, Canada. His research focuses on statistical and array signal processing for wireless communications and 5G-enabling technologies. He serves regularly as a TPC member for major IEEE conferences. He was a recipient of the very prestigious NSERC PDF Grant (2017–2018). He was also a recipient of the prestigious PDF Scholarship offered over the same period (but declined) from the Fonds de Recherche du Québec Nature et Technologies. He was awarded the INRS Innovation Award (2014–2015), a very prestigious Academic Gold Medal of the Governor General of Canada (2009–2010), and the Excellence Grant of the Director General of INRS (2009–2010). He received the award for the best M.Sc. thesis in INRS-EMT (2009–2010) the National Grant of Excellence from the Tunisian Government twice, both for the M.Sc. and Ph.D. programs. In 2011, he received the Merit Scholarship for Foreign Students from the Ministère de l'Éducation, du Loisir et du Sport of Quebec, Canada. He acts as a reviewer for many international scientific journals and conferences.



Usa Vilaipornsawai received the B.Eng. degree from the King Mongkut University of Technology Thonburi, Thailand, in 1997, the M.Sc. degree from Concordia University, in 2001, and the Ph.D. degree from McGill University, Montreal, QC, Canada, in 2009.

From 2009 to 2011, she was a Research Fellow at the Institute for Systems and Robotics, University of Algarve, Faro, Portugal, where she was involved in underwater acoustic communications for European FP7-ICT funded Underwater Acoustic

Network Project.

Since 2012, she has been with the Huawei Ottawa Research and Development Centre, where she is involved in 5G wireless system research and standard specification development.

Her research interests include multi-TRP cooperation, ultra-reliable low-latency communication, non-orthogonal multiple access, spectrally-contained waveforms, channel coding, receiver design for MIMO systems, and adaptive channel equalization.



Liqing Zhang received the B.E. and M.E. degrees from the Department of Electrical Engineering, University of Science and Technology of China (USTC), China, in 1986 and 1989, respectively, and the Ph.D. degree from the Department of Electrical Engineering, McGill University, Canada, in 2003. He was a Lecturer with USTC from 1989 to 1994, and also a Visiting Research Fellow with McGill University in 1995, and a Research Associate with McGill University from 1996 to 1999. He was with

Nortel Networks, Ottawa, Canada, from 2000 to 2007, and also with SOMA Networks, Ottawa, Canada, from 2008 to 2009, as a Technical Lead and System Architect for radio access system design on UMTS/CDMA2000, WiMAX, and LTE (2.5G/3G/4G) networks. Since 2010, he has been with the Canada Research Centre, Huawei Technologies, Ottawa, Canada, where he currently holds the position of Senior Staff Engineer and LTE/NR Design Expert, focusing on the 5G radio access research and standardization.

His research interests are in wireless communications, including communication and information theories, signal processing, PHY/MAC cross-layer design and optimization, grant-free and non-orthogonal multiple access, cooperative communications, and interference cancellation and co-ordination in heterogeneous networks. For the 5G research, he has co-authored the chapter of “Grant-Free Multiple Access Scheme” in the book *Multiple Access Techniques for 5G Wireless Networks and Beyond* Eds. M. Vaezi, Z. Ding, and H. V. Poor; Springer, 2018) and holds over 50 U.S. awarded patents and pending patent applications. He was a recipient of the Outstanding Inventor Award at Huawei CRC in 2017.



Peiyong Zhu (F'18) received the M.Sc. degree from Southeast University in 1985, and the Ph.D. degree from Concordia University in 1993.

Prior to joining Huawei in 2009, she was a Nortel Fellow and the Director of the Advanced Wireless Access Technology at the Nortel Wireless Technology Lab. She led the team and pioneered research 1070 and prototyping on MIMO-OFDM and multi-hop relay. Many of these technologies developed by the team have been adopted into LTE standards and 4G products.

She is currently leading 5G wireless system research at Huawei, where her work focuses on advanced wireless access technologies and has contributed to over 200 granted patents. She has given lectures and participated in panel discussions on 5G vision and enabling technologies. She has co-chaired various 5G workshops at the IEEE GLOBECOM. She is actively involved in 3GPP and IEEE 802 standards development. She served as the Guest Editor for the *IEEE Signal Processing Magazine* Special Issue on the 5G Revolution and the *IEEE JOURNAL ON SELECTED AREAS IN COMMUNICATIONS* Special Issue on Deployment Issues and Performance Challenges for 5G.

Dr. Zhu is a fellow of Huawei and a WiFi Alliance Board member.